

Integrated Multi-scale Model of Thermal Conductivity for Expanded Perlite Powder Vacuum Insulation Panels*

Ziyan Fu¹[0009-0002-5670-9118], Jorge Corker²[0000-0002-7155-4735], and Mizi Fan¹[0000-0002-6609-3110]

¹ College of Engineering, Design and Physical Sciences, Brunel University London, Uxbridge UB8 3PH, UK {ziyan.fu,mizi.fan}@brunel.ac.uk

² IPN Led&mat, Rua Pedro Nunes, 3030 199, Coimbra, Portugal jcorker@ipn.pt

Abstract. Vacuum Insulation Panels (VIPs) have emerged as a forefront solution in energy-efficient building materials. Expanded perlite (EP) stands out for its unique combination of low density, cost-effectiveness, and excellent thermal insulating properties among the myriad materials employed in VIPs. This study presents an integrated model utilizing analytical methods and finite element analysis (FEA) to simulate the heat transfer and predict the thermal conductivity of EP powder VIPs across varying gas pressures. It introduces a procedure to generate representative elementary areas (REAs) adaptable to various material characteristics; in comparing the simulation results to measurement values, the proposed model demonstrates reliable predictive performance from 0.0001 to 1 atm. The proposed model efficiently handles rapid thermal conductivity changes near atmospheric pressure, resolving distortion issues in other works. Based on the model results of REAs reflecting various material characteristics, we found that reducing the non-flake ratio of particles and decreasing the thickness of flake particles obstruct the heat transfer across all pressure ranges. When the thermal conductivity of the absolute solid is relatively high, it is advisable for the industry to prioritize applying finer grinding; conversely, efforts should be directed towards reducing the thickness of flake particles.

Keywords: Vacuum Insulation Panel · Expanded Perlite · Thermal Conductivity · Model · Heat Transfer.

1 Introduction

According to the European Commission Energy Department, buildings in the EU are responsible for 40% of total energy consumption, meanwhile 75% of the building stock is identified as energy-inefficient. Based on this context, the emphasis on sustainable building practices has spurred research into advanced

* Supported by European Union's Horizon 2020 research and innovation programme under Grant Agreement No. 869898.

insulation materials, notably Vacuum Insulation Panels (VIPs). VIPs are usually built with a rigid porous core and sealed in an envelope. By evacuating the core, VIPs create a vacuumed environment where gaseous conduction and convection are nearly eliminated and thus achieve an extremely low thermal conductivity [4–6]. The thickness of VIPs is significantly thinner than traditional materials, making it particularly advantageous in situations where space is limited but high thermal resistance is required [7, 8], for instance, refrigeration [1], construction [2], and transportation [3].

Expanded Perlite (EP) is obtained from natural perlite, a natural igneous or sedimentary rock, by crushing natural perlite ore, then treated at high temperatures at 760°C to 1100°C to expand, release moisture and crystallization water, and finally cooled to room temperature [12, 13]. Despite being a non-renewable resource, abundant natural perlite reserves and cost-effective production methods make EP a sustainable choice [14]. EP stands out for its insulation, lightweight and affordability, making it a key component of VIPs. Its composition [17], rich in silicates and metal oxides, ensures chemical stability and longevity [18, 19].

Scientists have amassed considerable achievements in thermal conductivity modelling for porous materials since engineers attempted to establish empirical models [20]. These endeavours have primarily resulted in two major categories of models: analytical models and numerical models [21]. Analytical models typically compartmentalize the effective thermal conductivity into four parts: solid heat transfer, gas heat transfer, radiative heat transfer, and the coupling effects [22]. Conversely, numerical models feed all parameters, including morphological and physical parameters, into the simulation together. Upon setting boundary conditions, these numerical models employ Finite Element Analysis (FEA) [23, 24], lattice Boltzmann methods (LBM) [25–27], or even Molecular Dynamics (MD) [28] for simulation.

Since the mean free path of gas molecules is inversely proportional to the gas pressure, the range of the Knudsen number of the fluid inside the porous material spans a large range, makes impossible to use a single-scale model to cover all the situations. The advantage of analytical models lies in only utilizing morphological statistical data, eliminating the need to reconstruct material microstructures for thermal conductivity prediction [1]. However analytical models are still powerless for highly coupled scenarios at near atmospheric pressure [21]. Numerical models do just the opposite. However, in scenarios where the gas pressure diminishes significantly, attributable to the diminution of fluidic properties and the concurrent amplification of particulate attributes, the gas exhibits transitional or free molecular flow characteristics and consequentially limits the application of numerical models in extremely low-pressure circumstances.

Combining models from both categories to overcome the limitations and provide accurate thermal conductivity predictions across lifetime pressure ranges, this research aims to integrate analytical and numerical approaches to develop a comprehensive model suitable for studying vacuum insulation panels, thereby advancing understanding and application in sustainable building practices.

2 Material and Methodology

2.1 Material

This study uses the EP filler Perlite 180 to build VIPs. The Scanning Electron Microscope (SEM) images of Perlite 180 are shown in Figure 1 left. Unlike those perlite particles without grinding shown in Figure 1 right [29], the characteristic bubble morphology of EP is no longer recognizable after fine grinding; only broken tiny plates with thicknesses from around 300nm to 1 μm can be found.

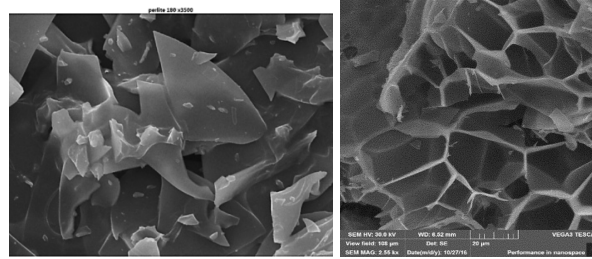


Fig. 1. SEM Images of Perlite 180 (left) and unground Perlite (right)

Due to the fine grinding, there are no closed pores within the Perlite 180 filler. The rule of mixtures with chemical composition analysis determines real density. This study calculates porosity through the ratio of the bulk density ($0.18\text{g}/\text{cm}^3$) to the real density ($2.796\text{g}/\text{cm}^3$) of EP powder. The resulting porosity is $\Pi = 1 - \frac{0.18\text{g}/\text{cm}^3}{2.796\text{g}/\text{cm}^3} = 93.56\%$.

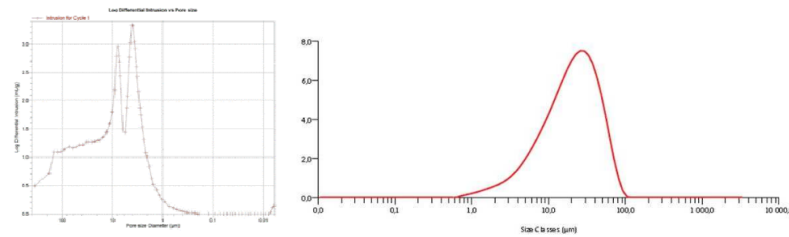


Fig. 2. Pore (left) and Particle (right) Diameter Distribution of Perlite 180

Another key parameter for VIP core materials is the diameter distribution of voids, which determines the vacuum levels required to keep the low thermal conductivity. From Figure 2, we can observe that the mode of the pore diameter distribution for Perlite 180 is just below $10\ \mu\text{m}$. This observation aligns with the situation presented in the SEM images.

Via laser diffraction technique, in reference to Figure 2, Perlite 180 displays a peak distribution centred at about 20 μm and the percentile data regarding particle diameter distribution is presented in Table 2. However, the laser diffraction technique is unsuitable for flake particles, which violates the assumption of spherical particles. Therefore, particle diameter results are only used for morphological analysis and will not be passed on to later simulations.

2.2 General Principles of Model Design

This section shows the analytical and numerical models used to investigate the effects of varying internal gaseous pressures on thermal conductivity due to ageing and damage. This study highlights the importance of the Knudsen number (Kn) [30], which helps determine the appropriate model based on gas behaviour in different pressure conditions. For $Kn < 0.1$, slip flow conditions are assumed, and a numerical model is applied. An analytical model based on rare gas theory is utilised for $Kn > 0.1$. The "divide and conquer" idea aims to provide a comprehensive model effective across a wide range of pressures.

2.3 Analytical Model for Lower Pressure

The thermal conductivity of porous media comprises three components: solid heat transfer, gas heat transfer, and radiative heat transfer [21]. In a rarefied gas environment ($Kn > 0.1$), where pressure is the only variable, solid heat transfer and radiative heat transfer can be considered constants. For scenarios where low-pressure results in a $Kn > 0.1$, we started with the classic Kaganer model, designed a more robust version of the Kaganer model, and applied it to the calculation of the thermal conductivity of gases within porous media [30]. Firstly, the Kaganer model is introduced with a parallel plates assumption: a gas with molecular mean free path l_g passing through two parallel plates at a distance D , and the equivalent gaseous thermal conductivity λ_{gas} can be calculated as:

$$\lambda_{gas} = (\Pi\lambda_0)/(1 + 2\beta Kn) = (\Pi\lambda_0)/(1 + 2\beta(l_g/D)) \quad (1)$$

where Π is the total porosity, λ_0 is the thermal conductivity of the gas in free space ($Kn < 0.01$), β is a dimensionless coefficient related to the gas accommodation and adiabatic coefficient and the coefficient β for air is 1.55. Kn is the ratio of l_g to D . l_g is defined as $l_g = (k_B T)/(\sqrt{2}\pi d^2 p)$, where k_B is the Boltzmann constant, T is the temperature, d is the diameter of a gas molecule and p is the gas pressure.

However, the average pore diameter D is not easy to determine from experimental results. From uniform pore size [30] to normal [31] and bimodal [32] normal distribution, scientists have been trying to model the pore size distribution of porous materials with distributions that are more consistent with experimental results. In this study, to restore the experimental results as well as mitigate the unevenly distributed sampling value and influence of outliers, we assume that the pore diameter d follows a lognormal distribution D :

$$f(d; \mu, \sigma) = \frac{1}{d\sigma\sqrt{2\pi}} e^{-\frac{(\ln d - \mu)^2}{2\sigma^2}} \quad (2)$$

where μ and σ are the mean (expectation) and standard deviation of lognormal distribution D . We then deduce the mean by reverse engineering through the more readily obtained mode and median.

The mean $E(D)$ conforming to the log-normal distribution can be calculated with the mode $\text{Mode}[D] = e^{\mu - \sigma^2}$ and the median $\text{Med}[D] = e^\mu$ as Equation 3:

$$E(D) = e^{\mu + \frac{\sigma^2}{2}} = \sqrt{e^{2\mu} e^{\sigma^2}} = \sqrt{\frac{e^{3\mu}}{e^{\mu - \sigma^2}}} = \sqrt{\frac{\text{Med}[D]^3}{\text{Mode}[D]}} \quad (3)$$

The mean pore diameter for Perlite 180 can be calculated as $E(D_{180}) = \sqrt{\frac{\text{Med}[D_{180}]^3}{\text{Mode}[D_{180}]}} = \sqrt{\frac{9.1\mu\text{m}^3}{4\mu\text{m}}} \approx 13.7\mu\text{m}$

Therefore, the effective thermal conductivity of EP powder under a rarefied gas environment can be summarized as:

$$\lambda_{analytical} = \lambda_{gas} + \lambda_{solid} + \lambda_{radiation} = \lambda_{gas} + \lambda_{const} = \frac{\Pi\lambda_0}{1 + 2\beta l_g \sqrt{\frac{\text{Mode}[D]}{\text{Med}[D]^3}}} + \lambda_{const} \quad (4)$$

where the sum of solid thermal conductivity λ_{solid} and radiative thermal conductivity $\lambda_{radiation}$ can be written as a constant variable λ_{const} .

2.4 Numerical Model for Higher Pressure

This study used SEM images of EP powder as a reference. We developed a visualized Grasshopper [33] program, enabling the generation of a Representative Elementary Area (REA) tailored to a specific set of characteristics for EP samples. Finally, the REAs and material's characteristic values are fed into the FEA slip flow model implemented by COMSOL Multiphysics. Meanwhile, we eliminate the influence of the randomness of REA generation on the final results by averaging multiple calculations.

Limit by the length of the short paper, we omit the details of generating REAs and only describe the design logic here. First, we randomly divide the REA into many cells with a diameter equal to the characteristic pore diameter (Figure 3 left). Then starting from the minimum observed wall thickness, we gradually increase the thickness until the porosity equals the observed value (Figure 3 middle). Finally, we hollowed out all vertices so that all solid walls were disjointed flakes (Figure 3 right).

In the subsequent finite element analysis, appropriate boundary conditions are established, and the physical properties of the gas and solid domains are incorporated into the model through empirical formulas or rules of mixtures. Finally, by utilizing the 2-dimensional thermal conductivity equation under appropriate sampling scope, the effective thermal conductivity of the REA is computed.

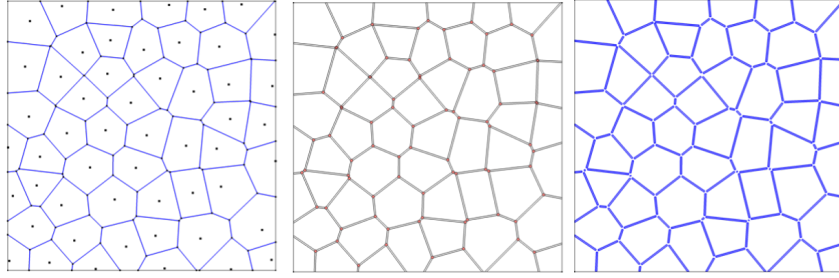


Fig. 3. Process of Constructing REA

As illustrated in Figure 4 left, the temperature difference between the 2 cm panel is $\Delta T_{2cm} = 5\text{K}$ at the macroscopic scale, and the temperature difference between the left and right sides of the REA at the microscopic scale is given by $\Delta T = \Delta T_{2cm} * L/20\text{mm} = 0.05\text{K}$. The initial temperature $T_{initial}$ of the REA is set as the medium temperature between the cold and hot plate $(T_{h_{2cm}} + T_{c_{2cm}}) / 2 = 295.65\text{K}$, and the temperature of cold (left) and hot (right) sides are $T_c = T_{initial} - \Delta T/2 = 295.625\text{K}$ and $T_h = T_{initial} + \Delta T/2 = 295.675\text{K}$. The top and bottom sides of the REA are periodic boundary conditions, in which heat and mass are allowed to transfer across the boundary periodically.

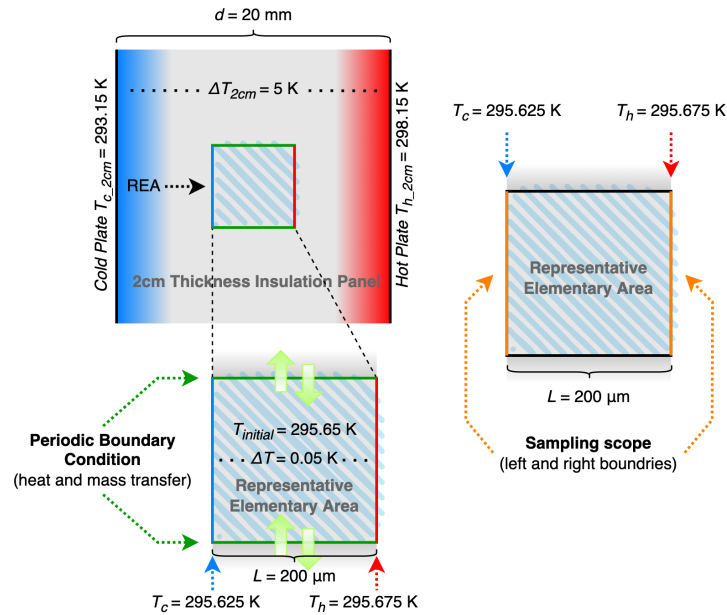


Fig. 4. Schematic Diagram and Sampling Scope of REA

In our research, the solid of the porous medium is expanded perlite, while the gas within the porous medium is dry air. For the gas domain, COMSOL Multiphysics provides built-in formulas for the physical properties of dry air.

For the solid domain, density, thermal conductivity, and heat capacity at constant pressure are required to perform the slip flow simulation. The rule of mixtures is applied to obtain the above parameters of the solid skeleton. By comparing numbers of the research paper, a representative composition of the EP solid (76% of SiO₂, 14% of Al₂O₃, 4% of Na₂O, 5% of K₂O and 1% of impurities) is assumed and will be applied with the rule of mixtures [34, 35].

As we know $\rho_{SiO_2} = 2648\text{kg/m}^3$, $\rho_{Al_2O_3} = 3987\text{kg/m}^3$, $\rho_{Na_2O} = 2270\text{kg/m}^3$, and $\rho_{K_2O} = 2130\text{kg/m}^3$. The density of EP solid ρ_{solid} is derived as:

$$\rho_{solid} = \sum \frac{m_i}{m_{mixture}} \rho_i = 2795.9\text{kg/m}^3 \quad (5)$$

Due to the lack of data in the academic community regarding the thermal conductivity of sodium oxide and potassium oxide as a function of temperature, we limit our consideration to the two primary components with the highest weight percentage in the EP solid: silicon dioxide and aluminium oxide. As we know $\lambda_{SiO_2} = 1.4\text{W/mK}$, $\lambda_{Al_2O_3} = 35\text{W/mK}$. The upper limit of thermal conductivity of EP solid λ_{solid} is derived as:

$$\lambda_{solid_upper} = \sum \frac{m_i}{m_{mixture}} \lambda_i = 6.627\text{W/mK} \quad (6)$$

The lower limit of thermal conductivity of EP solid λ_{solid} is derived as:

$$\lambda_{solid_lower} = \left(\sum \frac{m_i/m_{mixture}}{\lambda_i} \right)^{-1} = 1.646\text{W/mK} \quad (7)$$

As we know $C_{p_SiO_2} = 741.84\text{J}/(\text{kg} * \text{K})$ [38], $C_{p_Al_2O_3} = 753\text{J}/(\text{kg} * \text{K})$ [37], $C_{p_Na_2O} = 1114.71\text{J}/(\text{kg} * \text{K})$ [36], and $C_{p_K_2O} = 887.69\text{J}/(\text{kg} * \text{K})$ [39]. The heat capacity at a constant pressure of EP solid C_{p_solid} is derived as:

$$C_{p_solid} = \sum \frac{m_i}{m_{mixture}} C_{p_i} = 765.85\text{J}/(\text{kg} * \text{K}) \quad (8)$$

In our 2-dimensional simulation, the thermal conductivity of the REA is calculated with sampling on left and right boundaries (Figure 3 right): $\lambda = -\Phi * L / (T_h - T_c)$. Φ is the heat flux on sampling scope, L is the side length of square REA, T_h and T_c are the temperatures of the hot and cold sides of the REA, respectively.

2.5 Connection between Two Stages of Model

The analytical method and FEA slip flow model are exclusively utilized to address cases where the $\text{Kn} > 0.1$ and $\text{Kn} < 0.1$, respectively. For Perlite 180 (characteristic pore diameter = 13.7 μm), the boundary condition for $\text{Kn} = 0.1$ is $p_{boundary} = 0.05\text{atm}$. Therefore, we selected 0.005, 0.01, 0.02, 0.05, 0.1, 0.2, 0.5, and 1 atm as the scanning values for our FEA slip flow model, and take $p_{boundary}$

=0.05atm as the joint boundary of the coupled model. At the boundary pressure, the results of the analytical method $\lambda_{analytical_{0.05}}$ and the FEA slip flow model $\lambda_{FEA_{0.05}}$ should return the same value logically.

For Equation 4 utilized in the analytical method, λ_{const} is an unknown constant variable. Therefore, we apply the lower pressure boundary to the FEA slip flow model with $p = 0.05\text{atm}$ (i.e. when $Kn = 0.1$) and take the FEA model result $\lambda_{FEA_{0.05}}$ into Equation 9 to get the value of λ_{const} , then utilize Equation 4 to compute the effective thermal conductivity $\lambda_{analytical}$ when the gas pressure is lower than $p_{boundary}$.

$$\lambda_{FEA_{0.05}} = \lambda_{analytical_{0.05}} = \lambda_{const} + \frac{\Pi\lambda_0}{1 + 2\beta \frac{k_B T}{\sqrt{2\pi d^2 p_{boundary}}} \sqrt{\frac{Mod_e[D]}{Med[D]^3}}} \quad (9)$$

3 Model Results and Discussion

3.1 Results Validation

Validation of model hyperparameters ensures our FEA model results remain consistent regardless of the dimensions of REAs or mesh refinement. Firstly, the dimension of the REA needs to be validated to be large enough to endow the model with robustness against the randomness during the generation of the REA. The second to be validated is the level of mesh refinement during the finite element analysis since the model outcomes may fluctuate significantly with changes in mesh refinement.

To assess the convergence of FEA model outcomes regarding the dimension of the REAs, 7 dimensions ranging from 50 μm to 200 μm were evenly selected. Then, 5 different REAs were randomly generated for each dimension. The mean and the dispersion index of the model at all dimensions and pressure levels are monitored as follows:

$$\mu = \frac{\sum_1^n \lambda_i}{n}, \sigma^2 = \frac{\sum_1^n (\lambda_i - \mu)^2}{n}, D = \frac{\sigma^2}{\mu} \quad (10)$$

where σ^2 is the variance and μ is the mean.

Firstly, Figure 5 demonstrates that the mean of the model outcomes rapidly converges with increasing REA dimension from 50 μm to 125 μm . At dimensions greater or equal to 150 μm , the mean of the model outcomes is highly stable, exhibiting minimal variation with changes in REA dimension, and it can be considered as converged. Secondly, the dispersion index decreases significantly when the REA dimension increases from 50 μm to 125 μm . As long as the REA dimension is equal to or greater than 125 μm , even under atmospheric pressure (1 atm) conditions, the dispersion index of FEA model outcomes remains stable at less than 1%, which is a commendable and converged performance. In conclusion, the REA dimension should not be less than 150 μm , which is consistent with the argument presented in Chapter 3.

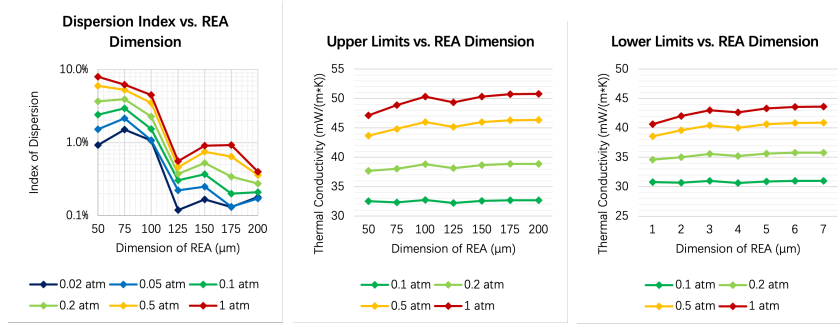


Fig. 5. Dispersion Index (left), Upper (middle) and Lower (right) Limits vs. REA Dimension

Secondly, to validate the reliability of the refinement level, in this section, we tested 7 mesh refinement levels: *Extremely Coarse*(- - -), *Extra Coarse*(- - -), *Coarser*(- -), *Coarse*(-), *Normal*(std), *Fine*(+) and *Finer*(++). The results of the above 7 refinement levels at 1 atm, 0.5 atm, and 0.1 atm are illustrated in Figure 6. Simulation results converge most rapidly during the refinement process from *Extremely Coarse* to *Coarser*, while they remain relatively stable during the refinement process from *Coarse* to *Finer*. We can conclude that the *Normal*(std) level of refinement level is sufficient and can be treated as a balance of the trade-off between accuracy and complexity.

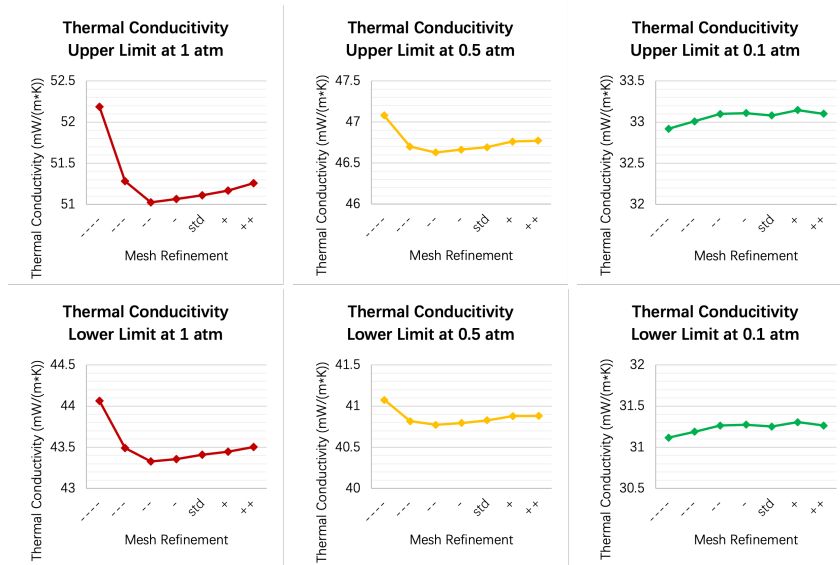


Fig. 6. Model Results at 1, 0.5 and 0.1 atm vs. Different Levels of Mesh Refinement

3.2 Results Comparison

From Figure 7, it can be observed that the divide-and-conquer approach adopted in this study has been successful. Within the range of relatively high pressures where slip flow can be applied, all measurement data fall within the thermal conductivity interval provided by our FEA model. The simulation results and experimental data exhibit notable consistency, showing a rapid increase in effective thermal conductivity and the logarithmic growth of pressure. In environments with even rarer gas, the analytical model and experimental data are generally in agreement and exhibit the same trends.

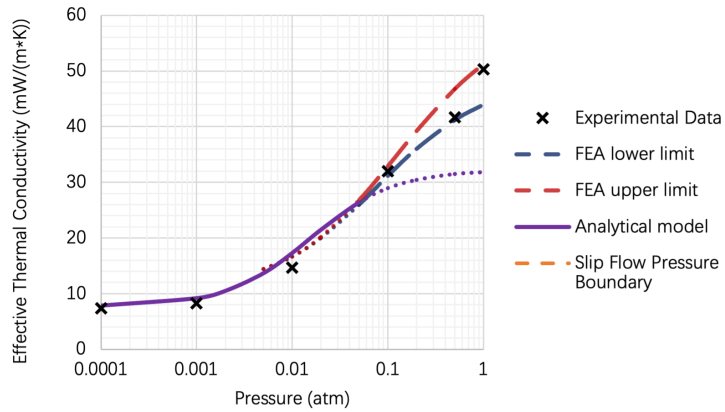


Fig. 7. Experimental Data and Results of Thermal Conductivity Models

Table 1. Experimental Data and Results of Thermal Conductivity Models

Pressure		Kn	FEA Model		Analytical model	Experimental data
atm	Pa		Upper Limit	Lower Limit		
			mW/(m*K)	mW/(m*K)	mW/(m*K)	mW/(m*K)
0.0001	10.1	10.1	/	/	7.85	7.4
0.001	101.3	5.06	/	/	9.18	8.3
0.002	202.6	2.54	/	/	10.5	/
0.005	506.6	1.01	14.416	14.399	13.67	/
0.01	1013.3	0.506	16.677	16.615	17.31	14.7
0.02	2026.5	0.254	20.178	19.977	21.5	/
0.05	5066.3	0.101	26.803	26.033	26.4	/
0.10	10133	0.0506	32.875	31.164	28.91	32
0.20	20265	0.0254	39.172	36.015	30.44	/
0.50	50663	0.0101	46.731	41.194	31.46	41.7
1.00	101325	0.00506	51.236	43.958	31.82	50.3

3.3 Discussion and Analysis

The study introduces an innovative model for predicting thermal conductivity in various materials, notably expanded perlite (EP) powder, within a range of gas pressures. Compared with existing similar research, this model stands out for two primary reasons. First, it adapts its approach based on the state of gas flow—accounting for different conditions like laminar flow, slip flow, and transitional flow—by incorporating methodologies specific to the Knudsen number (Kn). This "divide and conquer" strategy allows for a tailored and accurate representation of gas flow states without overcomplicating the model. Second, the model introduces a flexible generation of REAs, which can adapt to the microstructural variations of EP powders and other materials with similar characteristics. This adaptability is further enhanced by the model's ability to adjust for the absolute solid thermal conductivity based on the material's chemical composition, allowing for a precise representation of the material's thermal behaviour. Furthermore, this study not only offers insights into the thermal behaviour of EP powder but also proposes a framework applicable to a broader range of materials with similar structural characteristics.

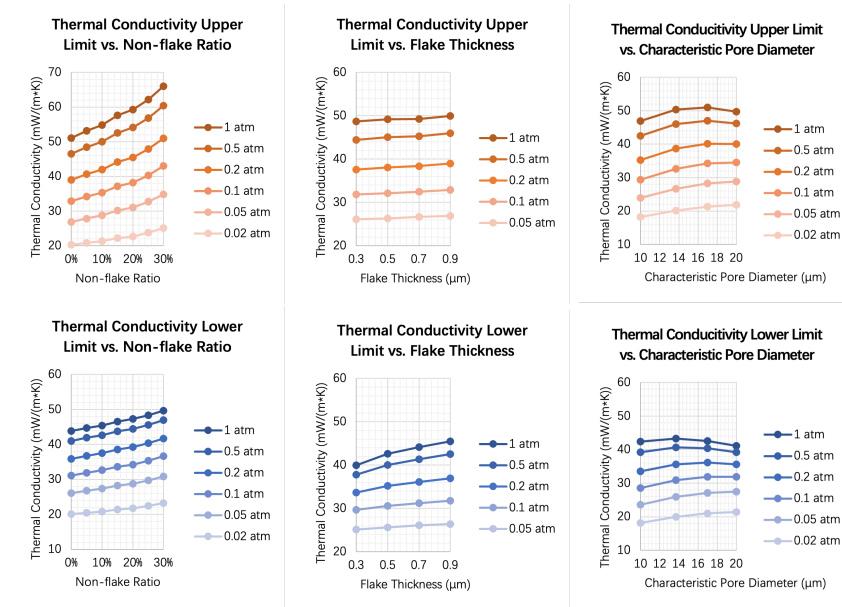


Fig. 8. Effective Thermal Conductivity Range vs. Non-flake Ratio (left), vs. Flake Thickness (middle), and vs. Characteristic Pore Diameter (right)

The study's findings demonstrate that an increase in the ratio of non-flake structures improves the effective thermal conductivity under all pressure conditions (Figure 8 left). Notably, this improvement is least significant at a pressure

of 0.02 atm when the solid's thermal conductivity is low. Additionally, the promotion of higher pressures to the enhancement is also noticed. We speculate that this is due to the intensified coupling effect between increased gas heat transfer at higher pressures and solid heat transfer in non-flake structures, amplifying the heat transfer increase resulting from changes in solid structure.

The flake thickness also serves as an essential parameter for predicting the effective thermal conductivity of EP powder under different pressures and it cannot be easily altered through physical methods such as grinding. It is evident that both the upper and lower limits of thermal conductivity increase with the growing flake thickness (Figure 8 middle). We infer that this phenomenon arises from the increase in the cross-sectional area of flakes due to the increased flake thickness, facilitating more heat flux transfer from the hot end to the cold end through the solid flake structure.

Lastly, Figure 8 (right) shows that the effect of characteristic pore diameter on the heat transfer of EP powder is non-monotonic, which warrants thorough discussion and analysis. Particularly at high pressures where gas heat transfer less significantly influences the overall thermal conductivity (Figure 8 right). The study suggests that the increase in pore diameter—and consequently, the mean free path of gas molecules—enhances gas thermal conductivity at lower pressures. However, with further increases in characteristic pore diameter, the porosity within the REA significantly increases. This leads to a significant reduction in the flaky solid structure to perform heat transfer, which not only offsets the thermal conductivity gain from the increase in the average size of flakes but also results in an overall decrease in effective thermal conductivity.

4 Conclusion

This study introduces a novel integrated model combining analytical methods with finite element analysis (FEA) to predict the thermal conductivity of vacuum insulation panels (VIPs) with expanded perlite powder across various gas pressures. Incorporating a Relative Effective Area (REA) adaptable to different pore sizes and porosities into the FEA, the model shows reliable predictive performance for pressures ranging from 0.0001 to 1 atm. It particularly addresses the distortion at high pressures seen in previous models, showcasing its robustness in handling rapid changes in effective thermal conductivity.

The investigation reveals that several factors influence the thermal conductivity of VIPs. A higher ratio of non-flake particles increases thermal conductivity, especially when the solid's thermal conductivity is enhanced. Flake particle thickness also impacts thermal conductivity, with variations more noticeable at lower solid thermal conductivities and higher pressures. The characteristic pore diameter's effect on heat transfer is complex, showing non-monotonic behaviour at high pressures but a monotonic increase in effective thermal conductivity with the diameter at low pressures.

To optimize VIPs' thermal performance, the study suggests finer grinding of perlite powder, reducing wall thickness chemically, and selecting appropriate

encapsulation pressures for optimal pore size. Future research could leverage the lattice Boltzmann method (LBM) for deeper insights into heat transfer in porous media like perlite powder at ultra-low pressures, enhancing understanding of material characteristics on thermal conductivity.

5 Data Availability

The processed data and program required to reproduce these findings are available to download from <https://gitlab.com/leo.ziyanfu/integrated-multi-scale-model-of-thermal-conductivity-for-expanded-perlite-powder-vacuum-insulation-panels.git>

References

1. Bouquerel, M., Duforestel, T., Baillis, D., Rusaouen, G.: Heat transfer modeling in vacuum insulation panels containing nanoporous silicas—A review. *Energy Build* **54**, 320-336 (2012).
2. Brunner, S., Ghazi Wakili, K., Stahl, T., Binder, B.: Vacuum insulation panels for building applications—Continuous challenges and developments. *Energy Build* **85**, 592-596 (2014).
3. Wang, B., Luo, R., Chen, H., Zheng, C., Gao, Y., Wang, H., Hashmi, A.R., Zhao, Q., Gan, Z.: Characterization and monitoring of vacuum pressure of tank containers with multilayer insulation for cryogenic clean fuels storage and transportation. *Appl. Therm. Eng.* **187**, 116569 (2021).
4. Corker, J., Marques, I., Resalati, S., Okoroafor, T., Maalouf, A., Fu, Z., Fan, M.: Al-rich industrial waste as new alternative of fumed silica for the manufacture of vacuum insulation panels for building energy conservation. *J. Clean. Prod.* **415**, 137854 (2023).
5. Raad, T., Verma, S., Singh, H.: Tree waste based advanced thermal insulation – Vacuum insulation panels – For application at up to 70 °C. *International journal of thermal sciences.* 200 (2024).
6. Zhuang, J., Ghaffar, S.H., Fan, M., Corker, J.: Restructure of expanded cork with fumed silica as novel core materials for vacuum insulation panels. *Composites.Part B, Engineering* **127**, 215-221 (2017).
7. Alam, M., Singh, H., Limbachiya, M.C.: Vacuum Insulation Panels (VIPs) for building construction industry – A review of the contemporary developments and future directions. *Appl. Energy.* **88**, 3592-3602 (2011).
8. Baetens, R., Jelle, B.P., Thue, J.V., Tenpierik, M.J., Grynning, S., Uvsløkk, S., Gustavsen, A.: Vacuum insulation panels for building applications: A review and beyond. *Energy Build.* **42**, 147-172 (2010).
9. Simões, N., Gonçalves, M., Serra, C., Resalati, S.: Can vacuum insulation panels be cost-effective when applied in building façades? *Build. Environ.* **191**, 107602 (2021).
10. Gonçalves, M., Simões, N., Serra, C., Flores-Colen, I.: A review of the challenges posed by the use of vacuum panels in external insulation finishing systems. *Appl. Energy.* **257**, 114028 (2020).
11. Mao, S., Kan, A., Zhu, W., Yuan, Y.: The impact of vacuum degree and barrier envelope on thermal property and service life of vacuum insulation panels. *Energy Build.* **209**, 109699 (2020).

12. Zhang, N., Yuan, Y., Yuan, Y., Li, T., Cao, X.: Lauric–palmitic–stearic acid/expanded perlite composite as form-stable phase change material: Preparation and thermal properties. *Energy Build.* **82**, 505-511 (2014).
13. Alam, M., Singh, H., Brunner, S., Naziris, C.: Experimental characterisation and evaluation of the thermo-physical properties of expanded perlite—Fumed silica composite for effective vacuum insulation panel (VIP) core. *Energy Build.* **69**, 442-450 (2014).
14. Rottmann, M., Beikircher, T., Ebert, H., Hemberger, F., Manara, J.: Thermal conductivity and extinction coefficient of opacified expanded perlite for vacuum super insulation up to 1073 K. *International journal of thermal sciences* **163**, 106813 (2021).
15. Reka, A.A., Pavlovski, B., Lisichkov, K., Jashari, A., Boev, B., Boev, I., Lazarova, M., Eskizeybek, V., Oral, A., Jovanovski, G., Makreski, P.: Chemical, mineralogical and structural features of native and expanded perlite from Macedonia. *Geologia Croaticam* **72**, 215-221 (2019).
16. Zukowski, M., Haese, G.: Experimental and numerical investigation of a hollow brick filled with perlite insulation. *Energy Build.* **42**, 1402-1408 (2010).
17. Singh, M., Garg, M.: Perlite-based building materials — a review of current applications, *Constr. Build. Mater.* **5**, 75-81 (1991).
18. Jia, G., Li, Z., Liu, P., Jing, Q.: Preparation and characterization of aerogel/expanded perlite composite as building thermal insulation material. *J. Non Cryst. Solids* **482**, 192-202 (2018).
19. Pichór, W., Janiec, A.: Thermal stability of expanded perlite modified by mullite. *Ceram. Int.* **35**, 527-530 (2009).
20. Bouquerel, M., Duforestel, T., Baillis, D., Rusaouen, G.: Mass transfer modeling in gas barrier envelopes for vacuum insulation panels: A review. *Energy Build.* **55**, 903-920 (2012).
21. Fu, Z., Corker, J., Papathanasiou, T., Wang, Y., Zhou, Y., Madyan, O.A., Liao, F., Fan, M.: Critical review on the thermal conductivity modelling of silica aerogel composites. *Journal of Building Engineering* **57**, 104814 (2022).
22. Kwon, J., Jang, C.H., Jung, H., Song, T.: Effective thermal conductivity of various filling materials for vacuum insulation panels. *Int. J. Heat Mass Transfer* **52**, 5525-5532 (2009).
23. Subramanian, G., Picu, C.R.: Mechanics of three-dimensional, nonbonded random fiber networks. *Phys Rev E.* **83**, 056120 (2011).
24. Liu, Q., Lu, Z., Hu, Z., Li, J.: Finite element analysis on tensile behaviour of 3D random fibrous materials: Model description and meso-level approach. *Materials Science and Engineering: A.* **587** 36-45 (2013).
25. Gruceliski, A.: LBM estimation of thermal conductivity in meso-scale modelling. *Journal of Physics: Conference Series* **760** 12005 (2016).
26. Qin, X., Cai, J., Zhou, Y., Kang, Z.: Lattice Boltzmann simulation and fractal analysis of effective thermal conductivity in porous media. *Appl. Therm. Eng.* **180** 115562 (2020).
27. Lu, J., Kan, A., Zhu, W., Yuan, Y.: Numerical investigation on effective thermal conductivity of fibrous porous medium under vacuum using Lattice-Boltzmann method. *International Journal of Thermal Sciences* **160**, 106682 (2021).
28. Toosi, M.H., Siavashi, M.: Two-phase mixture numerical simulation of natural convection of nanofluid flow in a cavity partially filled with porous media to enhance heat transfer. *Journal of molecular liquids* **238**, 553-569 (2017).
29. Pavlík, V., Bisaha, J.: Lightweight mortars based on expanded perlite. *Key Eng. Mater.* **776**, 104-117 (2018).

30. Kaganer, M.G., Moscona, A.: Thermal insulation in cryogenic engineering, Jerusalem: Israel program for scientific translations, Jerusalem (1969).
31. Bi, C., Tang, G.H., Tao, W.Q.: Prediction of the gaseous thermal conductivity in aerogels with non-uniform pore-size distribution. *Journal of Non-Crystalline Solids* **358**, 3124-3128 (2012).
32. Reichenauer, G., Heinemann, U., Ebert, H.-P.: Relationship between pore size and the gas pressure dependence of the gaseous thermal conductivity. *Colloids and Surfaces A: Physicochemical and Engineering Aspects* **300**, 204-210 (2007).
33. Rutten, D.: Grasshopper 3D. 1.0 (2014).
34. Damiyine, B., Guenbour, A., Boussen, R.: Adsorption of rhodamine b dye onto expanded perlite from aqueous solution: Kinetics, equilibrium and thermodynamics. *Journal of Materials and Environmental Science* **8**, 345-355 (2017).
35. Blaskov, V., Stambolova, I., Georgiev, V., Batakliiev, T., Eliyas, A., Shipochka, M., Vassilev, S., Mehandjiev, D.: Synthesis and Catalytic Activity of Silver-Coated Perlite in the Reaction of Ozone Decomposition. *Ozone: Sci. Eng.* **37** 252-256 (2015).
36. National Institute of Standards and Technology, Quartz (SiO₂), <https://webbook.nist.gov/cgi/cbook.cgi?ID=C14808607>, Last accessed 2024/03/01.
37. MatWeb, Corundum, Aluminum Oxide, Alumina, 99.9%, Al₂O₃, <https://www.matweb.com/search/DataSheet.aspx?MatGUID=c8c56ad547ae4cfabad15977bfb537f1>, Last accessed 2024/03/01.
38. National Institute of Standards and Technology, disodium oxide, <https://webbook.nist.gov/cgi/cbook.cgi?Formula=na2o>, Last accessed 2024/03/01.
39. National Institute of Standards and Technology, dipotassium oxide, <https://webbook.nist.gov/cgi/cbook.cgi?ID=12136457>, Last accessed 2024/03/01.